



HAL
open science

Redox- and solvato-magnetic switching in a tetrathiafulvalene-based triad single-molecule magnet

Fabrice Pointillart, Jessica Flores Gonzalez, Vincent Montigaud, Lorenzo Tesi, Vladimir K. Cherkasov, Boris Le Guennic, Olivier Cador, Lahcène Ouahab, Roberta Sessoli, Viacheslav Kuropatov

► To cite this version:

Fabrice Pointillart, Jessica Flores Gonzalez, Vincent Montigaud, Lorenzo Tesi, Vladimir K. Cherkasov, et al.. Redox- and solvato-magnetic switching in a tetrathiafulvalene-based triad single-molecule magnet. *Inorganic Chemistry Frontiers*, 2020, 7 (12), pp.2322-2334. 10.1039/d0qi00319k . hal-02928529

HAL Id: hal-02928529

<https://hal.science/hal-02928529>

Submitted on 22 Feb 2021

HAL is a multi-disciplinary open access archive for the deposit and dissemination of scientific research documents, whether they are published or not. The documents may come from teaching and research institutions in France or abroad, or from public or private research centers.

L'archive ouverte pluridisciplinaire **HAL**, est destinée au dépôt et à la diffusion de documents scientifiques de niveau recherche, publiés ou non, émanant des établissements d'enseignement et de recherche français ou étrangers, des laboratoires publics ou privés.

Redox- and Solvato-Magnetic Switching in a Tetrathiafulvalene-Based Triad Single-Molecule Magnet

Fabrice Pointillart,^{*a} Jessica Flores Gonzalez,^a Vincent Montigaud,^a Lorenzo Tesi,^{b,c} Vladimir Cherkasov,^d Boris Le Guennic,^a Olivier Cador,^a Lahcène Ouahab,^a Roberta Sessoli^b and Viacheslav Kuropatov^{*d}

^a Univ Rennes, CNRS, ISCR (Institut des Sciences Chimiques de Rennes) - UMR 6226, F-35000 Rennes, France.

^b Dipartimento di Chimica "Ugo Schiff" & INSTM RU, Università degli Studi di Firenze, Via della Lastruccia 3-13, I50019 Sesto Fiorentino (Firenze), Italy.

^c Institute of Physical Chemistry, University of Stuttgart, Pfaffenwaldring 55, 70569, Stuttgart, Germany.

^d G. A. Razuvaev Institute of Organometallic Chemistry of Russian Academy of Sciences, 603950, GSP-445, Tropinina str., 49, Nizhny Novgorod, Russia.

The first simultaneous redox and solvato-magnetic switching was achieved. The dinuclear complex $[\text{Dy}_2(\text{hfac})_6(\text{H}_2\text{SQ})]\cdot\text{CH}_2\text{Cl}_2$ (**Dy₂H₂SQ**) (where hfac = 1,1,1,5,5,5-hexafluoroacetylacetonate and **H₂SQ** = 2,2'-benzene-1,4-diylbis(6-hydroxy-4,7-di-tert-butyl-1,3-benzodithiol-2-ylidene-5-olate) was reversibly oxidized into the dinuclear complex $[\text{Dy}_2(\text{hfac})_6(\text{H}_2\text{O})_2(\text{Q})]$ (**Dy₂Q**) (where **Q** = 2,2'-cyclohexa-2,5-diene-1,4-diylidenebis(4,7-di-tert-butyl-1,3-benzodithiole-5,6-dione)) inducing the reversible coordination of water molecule to the Dy^{III} ion. Magnetic susceptibility measurements and *ab-initio* CASSCF/SI-SO calculations, confirmed by Cantilever Torque Magnetometry measurements, demonstrated that **Dy₂H₂SQ** is a Single-Molecule Magnet with a magnetic relaxation 7000 times slower than **Dy₂Q** (at 3 K) allowing a "ON-OFF" switching of the magnetic bistability.

Introduction

For the last three decades, Single-Molecule Magnets (SMMs), i.e. molecules that display slow magnetic relaxation, have been playing a key role in the field of molecular magnetism.¹ Indeed, such molecular objects have potential applications in high-density data storage,² quantum computing,³ and spintronics.⁴ Even more challenging than the sole observation of the SMM behavior in high temperature range,⁵ is a reversible control of the magnetic properties of SMMs, which could open promising additional applications such as switches and sensors.⁶ So far, such tuning of physical properties in SMMs has been achieved via crystal-to-crystal chemical transformations,⁷ solvato-switching,⁸ isomerization-switching,⁹ or redox-switching.¹⁰ The latter implies, most of the time, the use of redox active ligands leading to the design of multi-properties SMMs.

Focusing on the redox-switching, the use of multi-electro-active bridging ligands such as acceptor-donor-acceptor (A-D-A) triads is of particular interest because they cobble the route of magnetic modulation of the bridged magnetic active units through reduction of A or oxidation of D.¹¹ In this context, some of us already demonstrated that SMMs can be designed using redox active tetrathiafulvalene (TTF)-based ligands in its neutral

and oxidized forms.¹² In 2012, the synthesis and characterization of the $[\text{Dy}_2(\text{hfac})_6(\text{H}_2\text{O})_2(\text{L})]$ SMM was reported, in which the two Dy(hfac)₃ magnetic units are bridged by the 4,4',7,7'-tetra-tert-butyl-2,2'-bi-1,3-benzo-dithiole-5,5',6,6'-tetrone triad (**L**) involving both redox-active *o*-quinone (playing the role of A) and TTF moieties (playing the role of D).¹³ We wish now to go one step forward by designing new A-D-A triads with more powerful donor such as *p*-phenylene-extended TTF, i.e. the 2,2'-benzene-1,4-diylbis(6-hydroxy-4,7-di-tert-butyl-1,3-benzodithiol-2-ylidene-5-olate ligand (**H₂SQ**)).¹⁴ Such chemical modifications stabilize the doubly reduced deprotonated form of the ligand opening the possibility to play with its redox activity to modulate the magnetic properties of the corresponding complexes.

Herein we present details of the redox- and hence hydro-switching of the magnetic properties between the $[\text{Dy}_2(\text{hfac})_6(\text{H}_2\text{SQ})]\cdot\text{CH}_2\text{Cl}_2$ (**Dy₂H₂SQ**) and $[\text{Dy}_2(\text{hfac})_6(\text{H}_2\text{O})_2(\text{Q})]$ (**Dy₂Q**) (where **Q** = 2,2'-cyclohexa-2,5-diene-1,4-diylidenebis(4,7-di-tert-butyl-1,3-benzodithiole-5,6-dione). The redox-activity of the triads imposes the dehydration and rehydration of the Dy^{III} coordination sphere, which, in turn, modifies the magnetic anisotropy and thus the slow magnetic relaxation. The compounds were characterized by X-ray crystallography, SQUID magnetometry, Cantilever Torque Magnetometry (CTM) and *ab initio* CASSCF/SI-SO calculations.

Results and Discussion

Synthesis and X-ray diffraction analysis.

Compound **Dy₂H₂SQ** was prepared by reacting Dy(hfac)₃·2H₂O with purple **H₂SQ** in CH₂Cl₂ in aerobic conditions at room temperature. Blue single crystals of **Dy₂H₂SQ** were obtained by

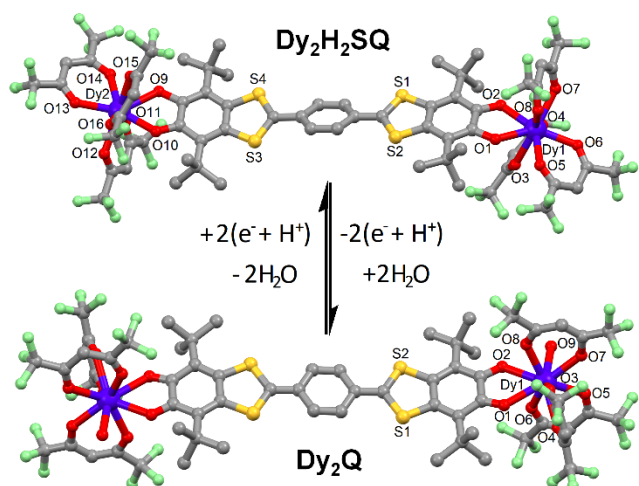
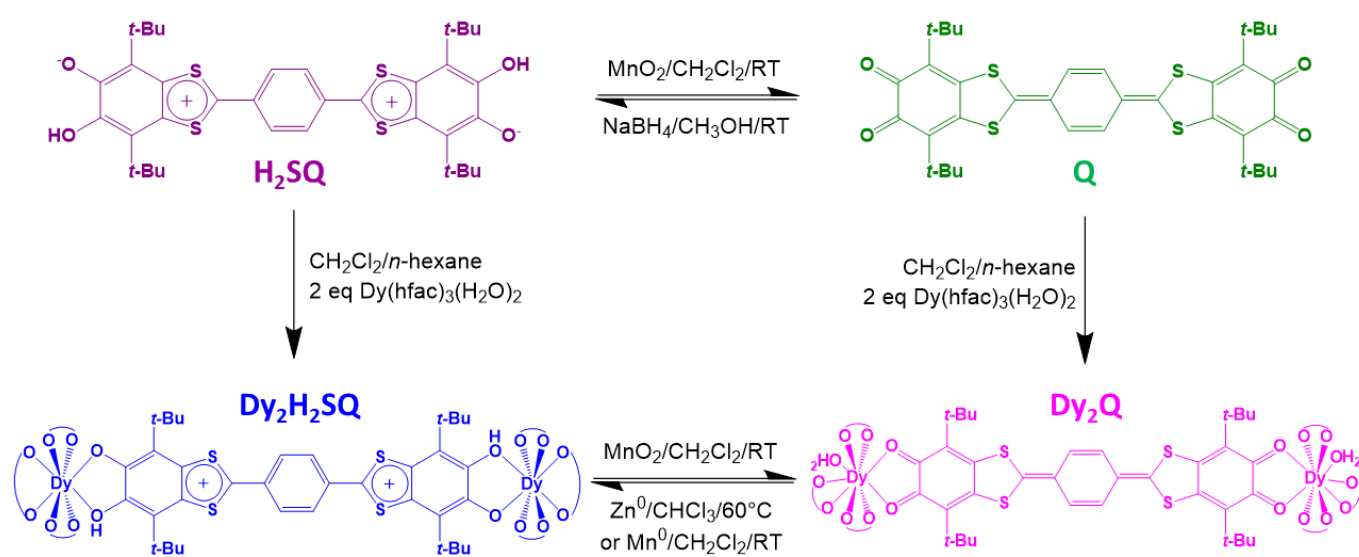


Fig. 1. Crystal structures of the dinuclear complexes $\text{Dy}_2\text{H}_2\text{SQ}$ (top) and Dy_2Q (bottom) connected by a redox and dehydration/rehydration reversible process.

layering *n*-hexane on the $\text{Dy}_2\text{H}_2\text{SQ}$ mother solution (Scheme 1) (See experimental part for Method A). It is worth noticing that $\text{Dy}_2\text{H}_2\text{SQ}$ can be obtained also by reduction of Dy_2Q with Zn^0 powder at 60°C in CHCl_3 or Mn^0 powder at room temperature in CH_2Cl_2 (Scheme 1) (See experimental part for Method B). Single-crystal diffraction (Table S1) revealed the formation of a dinuclear complex (Top of Fig. 1 and Fig. S1). Both Dy^{III} ions are linked to three *hfac*⁻ anions and to the doubly reduced diprotonated form of the triad, forming an O_8 coordination sphere with a D_{2d} triangular dodecahedron symmetry (SHAPE analysis,¹⁵ Table S2). The average $\text{Dy}-\text{O}_{\text{SQ}}$ and $\text{Dy}-\text{OH}_{\text{SQ}}$ distances are respectively shorter ($2.228(3)$ Å) and longer ($2.444(4)$ Å) than the $\text{Dy}-\text{O}_{\text{hfac}}$ bond length ($2.357(4)$ Å) giving a first indication of the bis monoprotonated form of the triad in $\text{Dy}_2\text{H}_2\text{SQ}$. Such form is also supported by the longer bond length of $\text{C}-\text{O}1/9$ ($1.377(6)$ Å) compared to $\text{C}=\text{O}2/10$ ($1.298(6)$ Å). An intramolecular electron transfer can take place between the

two protonated semiquinone structure (H_2SQa) and the charge-separated structure (H_2SQ) (Scheme S1). The 1,3-dithiole rings in $\text{Dy}_2\text{H}_2\text{SQ}$ is essentially aromatic since the $\text{S}1-\text{C}15$ ($1.679(5)$ Å), $\text{S}2-\text{C}15$ ($1.670(5)$ Å), $\text{S}3-\text{C}22$ ($1.677(5)$ Å) and $\text{S}4-\text{C}22$ ($1.668(5)$ Å) are comparable with those for TTF dications ($1.670-1.690$ Å) while they are longer in neutral TTF ($1.730-1.760$ Å).¹⁶⁻¹⁸ The dicationic character of the extended TTF induced a single character of the $\text{C}15-\text{C}16$ ($1.459(6)$ Å) and $\text{C}21-\text{C}22$ ($1.466(6)$ Å) bonds and thus allows a torsion angle of $23.4(1)^\circ$ between the 6-hydroxy-4,7-di-*tert*-butyl-1,3-benzodithiol and *p*-phenylene moieties.¹³ On balance, the X-ray structure is in favor of the charge-separated structure. The crystal packing revealed the formation of layers parallel to the $[110]$ plane and stacked together along the *c* axis (Fig. S2), while the dichloromethane molecules are localized between the layers. The shortest intra- and inter-molecular Dy-Dy distances are equal to 21.580 Å and 9.962 Å, respectively.

The oxidized form, Dy_2Q , could also be obtained by two methods. The first one consisted in the oxidation of H_2SQ with an excess of MnO_2 in CH_2Cl_2 at room temperature giving a deep green solution of Q . Then Q was in situ reacted with $\text{Dy}(\text{hfac})_3 \cdot 2\text{H}_2\text{O}$ in CH_2Cl_2 and crystallized by layering *n*-hexane, leading to the formation of dark pink single crystals of Dy_2Q (Scheme 1) (see Experimental part for Method A). The second method consisted in the direct oxidation of $\text{Dy}_2\text{H}_2\text{SQ}$ in the same conditions (Scheme 1) (See Experimental part for Method B). X-ray diffraction studies (Table S1) of Dy_2Q indicated the formation of a dinuclear complex in which the two Dy^{III} ions are coordinated by three *hfac*⁻ anions, one water molecule and the *o*-quinone moiety (bottom of Fig. 1 and Fig. S3). The trapped quinone form of the bridging ligand in Dy_2Q is remarkable since it was previously established that such a form cannot be isolated in solid-state due to its instability.¹⁴ In other words, the stability of Q is enhanced after complexation with the $\text{Dy}(\text{hfac})_3$ units.



Scheme 1. Synthetic Routes for obtaining the H_2SQ and Q ligands as well as the $\text{Dy}_2\text{H}_2\text{SQ}$ and Dy_2Q dinuclear complexes.

The resulting O_9 surrounding the Dy^{III} ion adopts a C_{4v} spherical capped square antiprism symmetry (Table S2). It is worth noticing that such an environment was also obtained with the **L** triad.¹³ In **Dy₂Q**, the average $Dy-O_o$, $Dy-O_w$ (where *w* indicates water) and $Dy-O_{hfac}$ distances are respectively 2.437(10) Å, 2.402(10) Å and 2.377(13) Å, while the $C=O1/2$ distances (1.227(18) Å) are in agreement with the quinone form. Quinone-like bond-lengths distribution in the 6-membered ring and the conformation of the ligand, which is now almost planar (torsion angle of 4.8(3)°), highlight the *p*-quinodimethane form of the central ring of the ligand **Q**.

The shortest Dy-Dy intramolecular distance is measured equal to 21.656 Å. Interestingly, the crystal packing shows the formation of a one-dimensional polymer thanks to hydrogen bonds between the coordinated water molecules and two *hfac* anions of the neighboring complex ($O9...O5 = 2.883$ Å and $O9...O2 = 2.868$ Å) (Fig. S4) leading to much shorter Dy-Dy intermolecular distances in **Dy₂Q** (6.071 Å) than in **Dy₂H₂SQ** (9.962 Å). Such hydrogen bonds strongly help the crystallization of **Dy₂Q** highlighting the importance of performing the chemical oxidation in non-anhydrous conditions. The neighboring chains are almost perpendicular, in contrast to the parallel arrangement previously observed in the dinuclear compound with **L**.¹²

Cyclic Voltammetry Analysis

The redox-activity was studied by measuring the cyclic voltammogram of **Dy₂H₂SQ** (Fig. S5). In the cathodic region, two close reduction processes, at -0.20 and -0.40 V, are observed and attributed to the successive reduction of the protonated semiquinone. A third reduction is also observed at -0.76 V, corresponding to the reduction of the central *p*-quinonoid spacer of the extended TTF.¹⁴ In the anodic region, two oxidation peaks are observed at +1.03 and +1.26 V, and they can be attributed to the oxidation of the protonated semiquinone. A comparison with the free **H₂SQ** ligand shows that the coordination of the two electronic withdrawing $Dy(hfac)_3$ moieties provoked a shift of +0.23, +0.17 and +0.15 V for the reduction potentials of the two protonated semiquinone and *p*-quinonoid moieties and a shift of +0.15 V for the oxidation potentials of the protonated semiquinone. This makes the reduction and the oxidation of the protonated semiquinone respectively easier and harder.¹⁴ Finally, it is worth remarking that the irreversible oxidation processes of the extended TTF into radical cation and dication species were observed at higher potentials for the free ligand.

Static Magnetic Measurements Analysis.

The static DC magnetic susceptibilities of **Dy₂H₂SQ** and **Dy₂Q** were measured from 300 K to 2 K (Fig. 2). At room temperature, both molecules display a $\chi_M T$ product (with χ_M being the molecular magnetic susceptibility and *T* the temperature in Kelvin) consistent with two-isolated Dy^{III} ions ($J=15/2$ and $g_J=4/3$) systems. Values of 27.7 $cm^3 K mol^{-1}$ and 28.4 $cm^3 K mol^{-1}$ are found for **Dy₂H₂SQ** and **Dy₂Q**, respectively. The monotonical decrease of the $\chi_M T$ vs *T* curve upon cooling is mainly attributed to thermal depopulation of the excited m_J states, while dipolar interactions, mainly of intermolecular

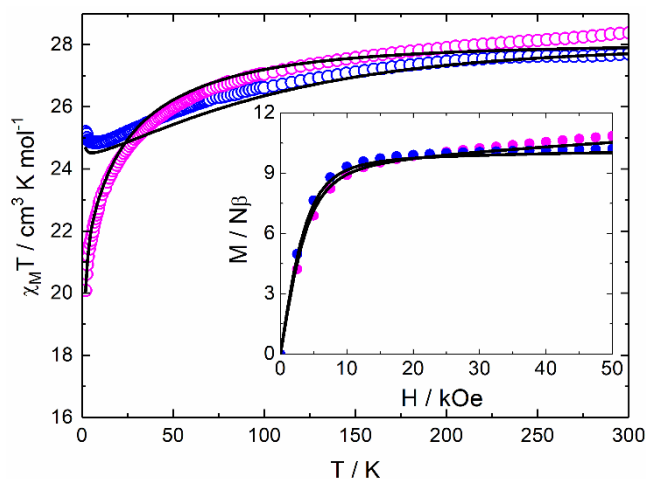


Fig. 2. Temperature dependence of $\chi_M T$ for **Dy₂H₂SQ** (open blue circles) and **Dy₂Q** (open pink circles). The inset shows the field variations of the magnetization at 2 K. The full black lines correspond to the simulated curves from *ab initio* calculations.

character, could be responsible for their different behavior at low temperature. Then, $\chi_M T$ vs *T* curve for **Dy₂H₂SQ** decreases monotonically to reach 24.8 $cm^3 K mol^{-1}$ at 6 K and ferromagnetic interactions may be responsible for the slight increase to 25.2 $cm^3 K mol^{-1}$ at 2 K. On the contrary, for **Dy₂Q**, the $\chi_M T$ vs *T* curve decreases monotonically to reach 20.1 $cm^3 K mol^{-1}$ at 2 K, indicating that antiferromagnetic interactions are dominating. At 2 K, the *M* vs *H* curve (with *H* the applied magnetic field) saturates at 10.2 $N\beta$ for **Dy₂H₂SQ**, which agrees with two pure Ising $m_J = \pm 15/2$ ground states for the Dy^{III} ions. For **Dy₂Q** the magnetization does not saturate at 50 kOe, highlighting a lack of anisotropy on the Dy^{III} ions (inset of Fig. 2).

Dynamic Magnetic Measurements Analysis.

Frequency dependent out-of-phase component of the ac susceptibility, χ_M'' , was observed for **Dy₂H₂SQ** between 2 and 22 K in a zero external magnetic field (Figs. 3a and S6). At 2 K, χ_M'' passes through a maximum at 25 Hz. The relaxation time τ was extracted at each temperature using an extended Debye

model (details in SI, Table S3) to fit simultaneously the frequency dependence of χ_M'' and of the in-phase susceptibility χ_M' (Fig. S7).

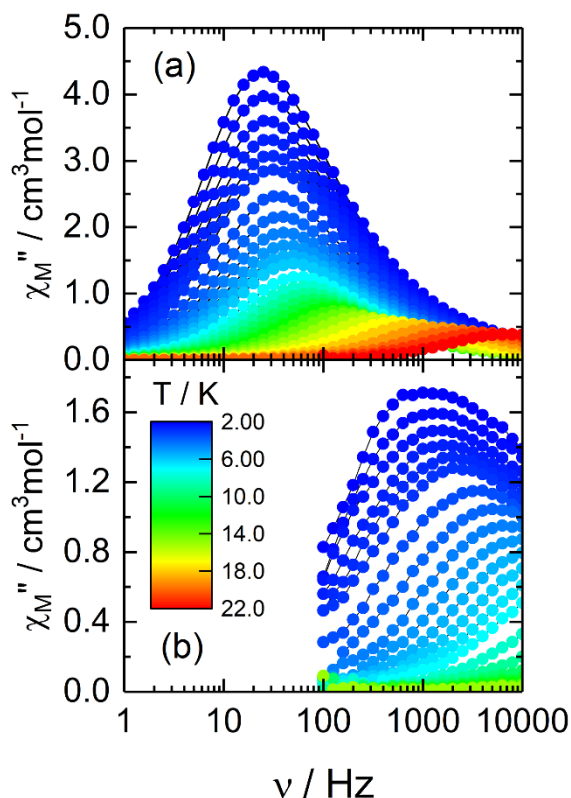


Fig. 3. Out-of-phase component of the AC magnetic susceptibility data for $\text{Dy}_2\text{H}_2\text{SQ}$ (a) and Dy_2Q (b) in zero-magnetic field between 2 and 22 K.

The normalized Cole-Cole plots in the temperature range 2 to 22 K are represented in Fig. S8. The resulting plots adopt a parabolic shape giving a narrow distribution of the relaxation times ($0.09 < \alpha < 0.25$). The relaxation time follows a combination of thermally dependent and thermally independent processes (Fig. 4). However, at low temperatures, the slight increase of τ can be due to the presence of small but sizeable interactions. Magnetic interactions, such as exchange/dipolar¹⁹ or hyperfine²⁰ effects, are known to modulate the thermally independent magnetic relaxations like Quantum Tunneling of the Magnetization, QTM, without affecting the thermally activated processes such as Orbach and Raman.²¹ All attempts to synthesize diluted samples to cancel the dipolar interactions have been unsuccessful. A scan field of χ_M'' and χ_M' vs. ν (Fig. S9) was performed at 2 K in order to suppress the QTM at low temperature.^{12a,22} Under the applied DC magnetic field of 1200 Oe value at which the slowest relaxation is observed (Figs. 5a and S10), the distribution of the relaxation time parameters α ranges from 0.07 to 0.34 (Fig. S11 and Table S4). Furthermore, such a field cancels the effect of weak interactions. Owing to the fact that the thermally dependent Orbach and Raman regimes are field independent,²³ the parameters for these processes for $\text{Dy}_2\text{H}_2\text{SQ}$ were kept constant going from $H = 0$ to $H = 1200$ Oe. They were evaluated by fitting simultaneously the in-field and zero-field Arrhenius plots.

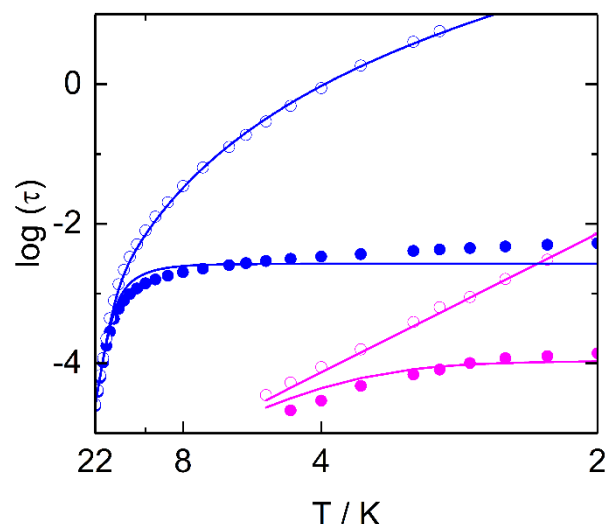


Fig. 4. Arrhenius plots of the relaxation times in zero magnetic field for $\text{Dy}_2\text{H}_2\text{SQ}$ (blue disks) and Dy_2Q (pink disks), and in a 1200 Oe applied magnetic field for $\text{Dy}_2\text{H}_2\text{SQ}$ (open blue circles) and Dy_2Q (open pink circles). Full lines are the best-fitted curves (see text).

The best fits were obtained considering both thermally dependent Orbach (green line, Fig. S12) and Raman (red line, Fig. S12) processes (equation 1)

$$\tau^{-1} = \underbrace{CT^n}_{\text{Raman}} + \underbrace{\tau_0^{-1} \exp\left(-\frac{\Delta}{KT}\right)}_{\text{Orbach}} + \underbrace{\tau_{\text{TI}}^{-1}}_{\text{QTM}} \quad \text{Eq. 1}$$

with $\Delta = 236(47)$ K, $\tau_0 = 5.7(51) \times 10^{-10}$ s and $C = 1.3(2) \times 10^{-3} \text{ s}^{-1} \text{ K}^{-n}$, $n = 4.85(10)$ for both $H = 0$ Oe and $H = 1200$ Oe magnetic fields between 2 and 22 K. The expected n value for Kramers ions should be 9,²⁴ but the presence of both acoustic and optical phonons could lead to lower values comprised between 2 and 7.²⁵ An additional thermally independent QTM process (blue line, Fig. S12) (Equation 1) was added in absence of applied magnetic field with $\tau_{\text{TI}} = 2.7(2) \times 10^{-10}$ s.²⁶ Passing to Dy_2Q , at zero external DC magnetic field, the χ_M'' vs. ν curve has a maximum close to 800 Hz at 2 K (Fig. S13), which is much faster than the value found for $\text{Dy}_2\text{H}_2\text{SQ}$ (25 Hz, *vide supra*). The application of a 1200 Oe DC field quenches the QTM (Fig. S14) and thus shifts the maxima to lower frequencies (Fig. S15). The two $\log(\tau)$ vs T curves were obtained by manual selection of the frequency maxima due to the broad shape of the out-of-phase signal of the susceptibility. The resulting Arrhenius plots were fitted using the same method previously adopted for $\text{Dy}_2\text{H}_2\text{SQ}$, i.e. simultaneous fitting the two Arrhenius plots obtained in- zero and in-field. The best fit for $H = 0$ Oe was obtained combining the thermally activated Orbach process for the high temperatures (green line, Fig. S16) with the temperature independent QTM (blue line, Fig. S16) process between 2 and 4.5 K (Fig. 4). The parameters extracted by the fit are $\Delta = 18.3(8)$ K, $\tau_0 = 7.6(2) \times 10^{-7}$ s and $\tau_{\text{TI}} = 1.1(1) \times 10^{-4}$ s. When a 1200 Oe static field is applied, the Arrhenius plot is fitted by considering a pure Orbach process and with the same parameters previously obtained. Thus, one could note that $\text{Dy}_2\text{H}_2\text{SQ}$ relaxes 7000 times slower than Dy_2Q at 3 K and under 1200 Oe. The hysteresis loops recorded at sub-kelvin temperatures highlight this difference. The loop is closed at any field at 0.5 K for Dy_2Q , whereas it is open with a butterfly shape for $\text{Dy}_2\text{H}_2\text{SQ}$ (Fig. 6).

Such behaviors are directly related to the different magnetic anisotropy of the Dy^{III} ion induced by the a D_{2d} O₈ (**Dy₂H₂SQ**) and C_{4v} O₉ (**Dy₂Q**) coordination environments, as well as by the different electronic distribution on surrounding ligands. This hypothesis is confirmed by *ab initio* calculations and single crystal magnetic investigations discussed in the following sections.

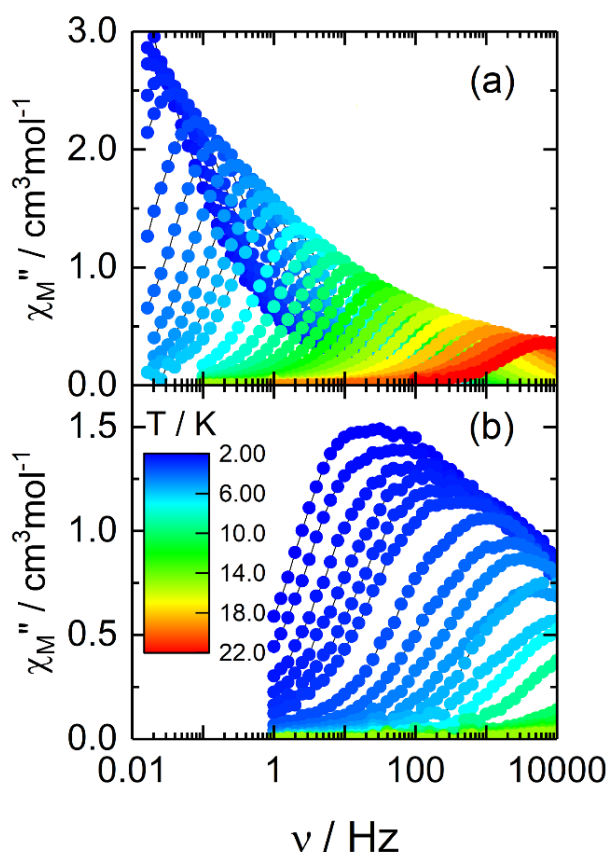


Fig. 5. Out-of-phase component of the AC magnetic susceptibility data for **Dy₂H₂SQ** (a) and **Dy₂Q** (b) in a 1200 Oe applied field

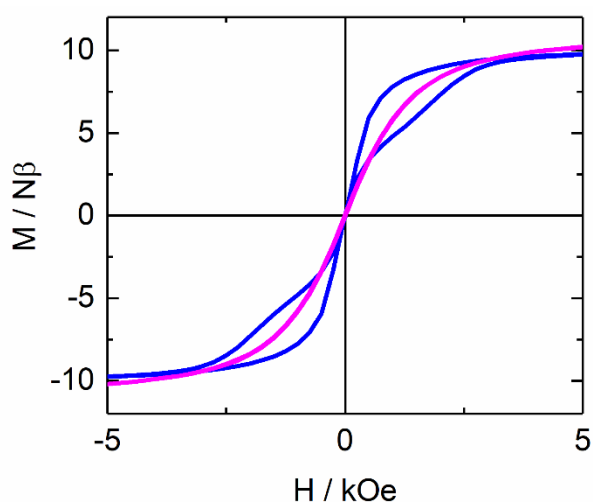


Fig. 6. Magnetic hysteresis loops at 0.5 K with a sweep rate of 16 Oe s⁻¹ for **Dy₂H₂SQ** (blue line) and **Dy₂Q** (pink line).

Theoretical Calculations and Cantilever Torque Magnetometry Measurements.

In order to propose a quantitative interpretation of the magnetic data, CASSCF/SI-SO *ab initio* calculations were performed on each asymmetric Dy^{III} center of complexes **Dy₂H₂SQ** and **Dy₂Q**, leading to the following models: [**Dy1HSQ**]⁻, [**Dy2HSQ**]⁻ and **DyQ** (Fig. 7; computational details in Experimental part). *Ab initio* calculations on [**Dy1HSQ**]⁻ and [**Dy2HSQ**]⁻ show very similar single-ion properties, with an almost Ising character of the ground state doublet (GD) magnetic anisotropy (Dy1: g_x = 0.00, g_y = 0.00 and g_z = 19.69; Dy2: g_x = 0.00, g_y = 0.00 and g_z = 19.70; Tables S5-S6). The ground state doublet is mainly composed of m_j = ±15/2 (97%).

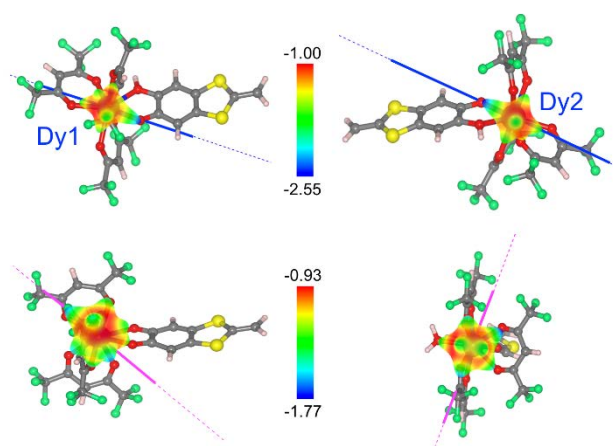


Fig. 7. Representation of the local ground state magnetic anisotropy axes and molecular electrostatic potential for [**Dy1HSQ**]⁻ and [**Dy2HSQ**]⁻ (top) and for **DyQ** (bottom, views from the side and along the ligand).

For both Dy^{III} centers, the orientation of the main anisotropy axes is calculated along the deprotonated O2 and O10 atoms (Fig. 7). The analysis of the molecular electrostatic potential, using our home-made code CAMMEL (description in the Experimental part), reveals that this orientation corresponds to the most-negatively charged potential.²⁷⁻²⁹ From this electrostatic distribution one may notice the strong anisotropy of the total molecular electrostatic potential along the non-protonated semiquinonate O atom of the extended-TTF ligand, which shows the shortest Dy-O distance of 2.23 Å, while the second O atom lies at 2.44 Å from the metal.

In order to validate results of the *ab initio* calculations, angular resolved magnetic measurements on a single crystal of **Dy₂H₂SQ** were performed using Cantilever Torque Magnetometry (CTM). Indeed, such a technique allows the experimental determination of both the magnitude and orientation of the magnetic anisotropy.³⁰ In general, the single crystal is mounted on the cantilever, acting as a capacitor plate. The cantilever can be rotated inside the DC applied magnetic field and θ defines the rotation angle, i.e. the angle between the cantilever plane and the direction of the magnetic field. The measured physical quantity is the change in capacitance due to the deflection of the cantilever's plate produced by the

magnetic torque of the sample. This measured quantity is indeed proportional to the magnetization torque, τ_{Mag} along the rotation axis, which corresponds to the vector product between the magnetization \mathbf{M} and the applied magnetic field \mathbf{H} . In the low-field limit $g\mu_{\text{B}}JH \ll k_{\text{B}}T$ the resulting curve has a sinusoidal behavior:

$$\tau_Y = M_Z H_X - M_X H_Z = H^2(\chi_{ZZ} - \chi_{XX}) \sin \eta \cos \eta \quad \text{Eq. 2}$$

where XYZ is the laboratory reference frame with the rotation performed around the Y-axis, while χ is the susceptibility tensor and η the angle between the projection of the molecular anisotropy principal axis in the XZ plane and the direction of the applied magnetic field \mathbf{H} .

According to Eq. 2, each time one of the principal anisotropy magnetic axes of the molecule, or its projection in the scanned plane, is parallel to the magnetic field vector, then τ_{Mag} is zero. In the high magnetic field regime, i.e., $g\mu_{\text{B}}JH \gg k_{\text{B}}T$ the torque changes more steeply when the magnetic field is close to the hard direction of the magnetic anisotropy. This effect enables us to disentangle the non-collinear contributions, such as those provided by different magnetic centers in the molecule.³¹ The orientation of the anisotropy can be solved probing two different crystallographic planes.

The measurements were performed on a single crystal of $\text{Dy}_2\text{H}_2\text{SQ}$ with dimensions 0.5x0.5x0.1 mm. The crystal was mounted on an acetate foil, which in turn was placed on the cantilever plate (see Fig. S17 for details on the orientation). In Rotation 1, the rotation axis Y was parallel to the crystallographic axis c^* , thus the magnetic field scanned the ab plane. Rotation 2 was instead performed along the vector normal to the $[\bar{2} 15 0]$ face, i.e. between the a and b axes. In this rotation the field was parallel to $-c^*$ at $\theta=0^\circ$. The measurements were performed at several temperatures between 2 and 50 K and varying the magnetic field between 3 and 12 T (Figs. 8 and S18-19). Fig. 8 reports the results of the measurements at 2 K for the two rotations and magnetic field values between 3 and 9 T. In Rotation 1, the first zero is found at 75° , that corresponds to the crystallographic axis a parallel to the magnetic field; looking at the asymmetric shape of the curves it is clear that the direction a has an easy axis character. After 90° , i.e. at 165° , a second zero is found and it corresponds to the hard axis b parallel to the magnetic field. These findings agree with the fact that b is also the C_2 -symmetry axis of the $P2_1/c$ space group, and it must coincide with one of the principal anisotropy axes of the crystal. Instead, in Rotation 2 no symmetry constraints are present. The first zero is at 27° and it has a hard character, whereas the second is at 117° with an easy character. It is worth pointing out that in this case, fits of torque magnetization are not trivial because of the significant number of parameters that over-parametrize the problem. Indeed, even in the simplest case, which corresponds to the pseudo-spin $\frac{1}{2}$ approximation, the modellization of the problem requires to find the ψ , ξ , and ρ Euler angles that connect the crystallographic abc^* and molecular xyz frames, in addition to the g_x , g_y and g_z values. Moreover, since the two Dy^{III} centers of the $\text{Dy}_2\text{H}_2\text{SQ}$ molecule are not equivalent, the parameters of

the fits must be considered twice for a total of 12 parameters. For this reason, only simulations based on the parameters obtained by *ab initio* calculations were performed.

The simulation of the torque magnetization for 2 K has been made considering both the pseudo-spin $\frac{1}{2}$ approximation (solid lines in Fig. S18) and the full Hamiltonian with all the 27 crystal field parameters (Fig. 8). In both cases, the parameters obtained from *ab initio* calculations well-reproduce the experimental curves. Indeed, the values of θ at which $\tau_{\text{Mag}} = 0$ occurs are always in agreement with the experimental findings. This indicates that the principal magnetic anisotropy directions, as well as the composition of the crystal field parameters, for the two Dy^{III} centers, are well-computed.

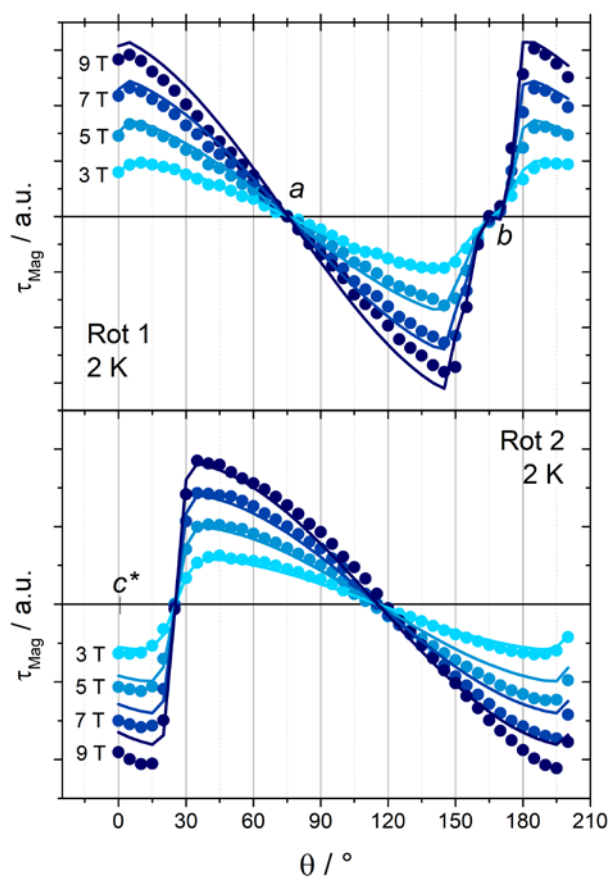


Fig. 8. Angular dependence of the magnetic torque (dots) of a single crystal of $\text{Dy}_2\text{H}_2\text{SQ}$ measured using Cantilever Torque Magnetometry at 2 K and under several applied DC magnetic fields. Rotation 1 (top) and 2 (bottom) were performed following the scheme reported in Fig. S17. Simulations (solid lines) were obtained considering the full Hamiltonian parameters obtained by *ab initio* calculations.

It must be underlined that the simulation is even able to reproduce the small plateau observed around 165° , which comes out from the symmetry nature of the b axis. The intensity of τ_{Mag} is also a key indicator of the quality of the simulations. It should be noted that a scale factor is applied, which takes into account the mass of the sample and other instrumental parameters, but this factor is unique for all data reported here. Remarkably, the agreement is maintained even extending the

experiment and simulation up to 50 K (Fig. S19), thus evidencing the robustness and accuracy of the *ab initio* calculations.

In the case of **Dy₂Q**, the calculations on the single asymmetric center reveal a much smaller splitting of the ⁶H_{15/2} multiplet. The presence of low lying excited states leads to a decrease of the ground doublet (GD) magnetic anisotropy with non-zero transversal components ($g_x = 0.07$, $g_y = 0.08$) and lower main component ($g_z = 18.93$). However, the composition of the GD remains mainly of $m_j = \pm 15/2$ (89%) character (Table S7). The computed orientation of the GD magnetic axis of **DyQ** appears along the O atoms of the “axial” hfac ligands, perpendicular to the plane containing the quinone moiety (Fig. 7). Such a shift of the magnetic axis might be ascribed to the coordination of the water molecule in the coordination sphere of the Dy^{III} ion and the deprotonation of the extended-TTF ligand, leading to an increase of the Dy-O distance from 2.23 Å (deprotonated) to 2.42 Å (protonated). Such a modification in the coordination sphere has a direct effect on the molecular electrostatic potential which shows a more “isotropic” distribution of the potential around the metal center. This variation is also evidenced by the different components of the total molecular electrostatic potential (Figs. S20 and S21). In both systems, the decomposition of the total electrostatic potential reveals a major contribution from the quadrupolar term, a trend already observed in previous works.^{29,32}

The computation of the single-ion anisotropy barriers of [**Dy1HSQ**]⁻ and [**Dy2HSQ**]⁻ are shown in Fig. S22.³³ The calculated transition elements of the magnetic moment, between the states lying at 300 cm⁻¹ from the GD, show a main relaxation pathway leading to an effective energy barrier equals to 280 cm⁻¹ (403 K), with the crossing at the second excited doublet.⁶ Such a value is far from the experimentally determined barrier height of 164 cm⁻¹ (236 K). In the case of **DyQ**, non-negligible QTM and TA-QTM coefficients are observed, explaining the fast relaxation behavior observed experimentally (Fig. S23).

From this “local” description (considering a single magnetic center) of the magnetic properties, one may see an excellent agreement between the experimental and calculated field dependence of the magnetization (Inset of Fig. 2). On the contrary the χ_{MT} vs. T curve at low temperature is not reproduced properly (Figs. S24 and S25). Such a discrepancy between calculations and experiments is often ascribed to weak inter/intramolecular interactions between the magnetic centers in the crystal. The increase observed in the low temperature range of the χ_{MT} vs. T curve of **Dy₂H₂SQ** suggests predominant ferromagnetic interactions. In the case of **Dy₂Q**, the sharp decrease of the magnetic susceptibility is, on the contrary, indicative of dominant antiferromagnetic interactions. Due to the complexity of the bridging ligands and the large distance between the magnetic centers, the intramolecular exchange term is not considered in this study. Therefore, the different behavior can be rationalized by assuming that only dipolar interactions are active between Dy^{III} centers. As implemented in the POLY_ANISO software,³⁴ in the pseudospin $\tilde{S}_i = 1/2$ formalism the dipolar interaction can be modelled with the following interaction Hamiltonian:

$$H_{int} = - \sum_i^N J_i \tilde{S}_i \tilde{S}_j$$

where J_i corresponds to the dipolar coupling constant between center i and j while \tilde{S}_i denotes the effective spin of center i . The pairwise contributions to the total interaction Hamiltonian considered in the calculations are depicted in Fig. S26 and Fig. S27 and correspond to the sphere containing the first magnetic neighbors of **Dy₂H₂SQ** and **Dy₂Q**, respectively.

In the case of **Dy₂H₂SQ**, the two asymmetric Dy^{III} centers exhibit very similar magnetic environment leading to two types of intermolecular interactions, namely Dy1-Dy1 (Dy2-Dy2) and Dy1-Dy2 interactions. The latter exhibit larger J values due to the shorter Dy1-Dy2 distances in the crystal (Table S8). One may notice that both weak Dy1-Dy2 intramolecular and Dy1-Dy1/Dy2-Dy2 intermolecular dipolar interactions are in the same range of values. The overall description of the magnetic environment of **Dy₂H₂SQ** is dominated by the major ferromagnetic contributions of Dy1-Dy2 interactions leading to the increase of the χ_{MT} product at low temperatures. The computation of the DC magnetic properties including such interactions is shown in Fig. 2 and reproduces the experimental trend of the χ_{MT} curve.

A similar computational approach was then considered for **Dy₂Q**, with a single type of intermolecular Dy-Dy interaction. One may see, from Fig. S25 and Table S9, that the shortest Dy-Dy distance (6.07 Å) leads to the largest antiferromagnetic $J_1 = -0.65$ cm⁻¹ constant. All the other contributions (intramolecular and intermolecular) lies one order of magnitude below J_1 , which is explained by the much larger Dy-Dy distances. The computation of this major term in the DC magnetic properties leads to a better description of the low temperature behavior (Fig. 2).

Conclusions

Starting from the dinuclear complex **Dy₂H₂SQ** involving the **H₂SQ** triad, the reversible chemical oxidation of **H₂SQ** into **Q** leads to the new dinuclear complex **Dy₂Q**. Both complexes are characterized by X-ray diffraction on single crystal. The reversible oxidation induces strong changes in the coordination sphere of the Dy^{III} ions with the addition of a water molecule. These structural and electronic evolutions are at the origin of drastic modulations of the magnetic relaxation in such way that **Dy₂H₂SQ** displays magnetic bistability while **Dy₂Q** does not. Cantilever Torque Magnetometry measurements confirmed the rationalization of the magnetic behavior using *ab-initio* CASSCF/SI-SO calculations. The change in magnetic anisotropy is also responsible of a change in the sign of the dominating intermolecular dipolar interactions. In conclusion, a simultaneous reversible redox and solvato-magnetic switching is here evidenced. Besides, the **H₂SQ** triad can be reversibly reduced in **H₄CAT** (CAT: catechol)^{35,36} which could open the route to novel redox-switching of the SMM behavior.

Experimental section

Materials. The precursor $\text{Dy}(\text{hfac})_3 \cdot 2\text{H}_2\text{O}$ ($\text{hfac}^- = 1,1,1,5,5,5$ -hexafluoroacetylacetonate anion)³⁷ and the 2,2'-benzene-1,4-diylbis(6-hydroxy-4,7-di-tert-butyl-1,3-benzodithiol-2-ylidene-5-olate triad (H_2SQ)¹⁴ were synthesized following previously reported methods. All solvents were dried using standard procedures. All other reagents were purchased from Aldrich Co., Ltd. and used without further purification.

Synthesis of $[\text{Dy}_2(\text{hfac})_6(\text{H}_2\text{SQ})] \cdot \text{CH}_2\text{Cl}_2$ ($\text{Dy}_2\text{H}_2\text{SQ}$).

Method A: 65.8 mg of $\text{Dy}(\text{hfac})_3 \cdot 2\text{H}_2\text{O}$ (0.08 mmol) were dissolved in 10 mL of CH_2Cl_2 and then added to a purple solution of 10 mL of CH_2Cl_2 containing 26.4 mg of H_2SQ (0.04 mmol). The purple solution of H_2SQ immediately turned blue with the addition of the Dy^{III} salt. After 15 minutes of stirring, 20 mL of *n*-hexane were layered at room temperature in the dark. Slow diffusion led to dark blue single crystals of $\text{Dy}_2\text{H}_2\text{SQ}$ that are suitable for X-ray diffraction studies. Yield (determined from isolated single crystals) 73.3 mg (79 %). Anal. Calcd (%) for $\text{C}_{67}\text{H}_{50}\text{Cl}_2\text{Dy}_2\text{F}_{36}\text{O}_{16}\text{S}_4$: C 34.67, H 2.16; found: C 34.69, H 2.22. I.R. (KBr): 2966 (w), 2928 (w), 2878 (w), 1651 (s), 1558 (w), 1533 (m), 1507 (m), 1422 (s), 1412 (s), 1388 (s), 1257 (s), 1205 (s), 1146 (s), 1103 (w), 801 (m), 662 (m), 585 (m) and 468 (m) cm^{-1} .

Method B: 22.6 mg of single crystals of Dy_2Q (0.01 mmol) were dissolved in 30 mL of CH_2Cl_2 and 2 g of reducing Mn^0 powder was added and then the mixture was stirred 2 h at room temperature under an argon atmosphere. After filtration and addition of *n*-hexane, single crystals of $\text{Dy}_2\text{H}_2\text{SQ}$ were obtained. Yield (determined from isolated single crystals) 5.3 mg (23 %). When Zn^0 is used as reducing agent, the CH_2Cl_2 is replaced by CHCl_3 and the mixture is stirred at 60 °C instead of room temperature.

Synthesis of $[\text{Dy}_2(\text{hfac})_6(\text{H}_2\text{O})_2(\text{Q})]$ (Dy_2Q).

Method A: 13.2 mg of H_2SQ (0.02 mmol) were dissolved in 20 mL of CH_2Cl_2 and then stirred in presence of 1.5 g of MnO_2 . The starting purple solution turned green (oxidation of H_2SQ into Q) and after 45 min of stirring it was filtered directly in a CH_2Cl_2 solution (5 mL) of $\text{Dy}(\text{hfac})_3 \cdot 2\text{H}_2\text{O}$ (32.8 mg, 0.04 mmol). The green solution turned to a dark pink color. Slow diffusion of *n*-hexane into the resulting dark pink solution led to formation of dark pink single crystals of Dy_2Q which were suitable for X-ray analysis. Yield (determined from isolated single crystals) 32.2 mg (71 %). Anal. Calcd (%) for $\text{C}_{66}\text{H}_{46}\text{Dy}_2\text{F}_{36}\text{O}_{18}\text{S}_4$: C 34.98, H 2.03; found: C 35.09, H 2.15. I.R. (KBr): 2964 (w), 2927 (w), 2861 (w), 1654 (s), 1532 (s), 1422 (s), 1395 (m), 1363 (m), 1256 (s), 1203 (s), 1146 (s), 1103 (w), 942 (m), 915 (m), 854 (m), 799 (m), 769 (m), 662 (m), 585 (m), 548 (m) and 529 (w) cm^{-1} .

Method B: Dy_2Q can be directly obtained by oxidation of the complex $\text{Dy}_2\text{H}_2\text{SQ}$. 22.6 mg of Dy_2Q (0.01 mmol) were dissolved in 20 mL of CH_2Cl_2 and then stirred in presence of 1.5 g of MnO_2 . The starting blue solution turned dark pink (oxidation of $\text{Dy}_2\text{H}_2\text{SQ}$ into Dy_2Q). Slow diffusion of *n*-hexane into the resulting dark pink solution led to formation of dark pink single crystals of Dy_2Q which were suitable for X-ray analysis. Yield (determined from isolated single crystals) 14.4 mg (62 %).

Characterization. The elemental analyses of the compounds were performed at the Centre Régional de Mesures Physiques de l'Ouest, Rennes. Cyclic voltammetry was carried out in dried and degassed CH_2Cl_2 solution, containing 0.1 M $\text{N}(\text{C}_4\text{H}_9)_4\text{PF}_6$ as

supporting electrolyte. Voltammograms were recorded at 100 mVs^{-1} at a platinum disk electrode. The potentials were measured *versus* a saturated calomel electrode (SCE).

X-ray diffraction study. Single crystals of $\text{Dy}_2\text{H}_2\text{SQ}$ and Dy_2Q were mounted on a APEXIII D8 VENTURE Bruker-AXS diffractometer for data collection (MoK_α radiation source, $\lambda = 0.71073$ Å), from the Centre de Diffractométrie (CDIFX), Université de Rennes 1, France (Table 1). The structure was solved with a direct method using the SHELXT program³⁸ and refined with a full matrix least-squares method on F^2 using the SHELXL-14/7 program³⁹. A SQUEEZE procedure of PLATON⁴⁰ was performed as the structure for Dy_2Q contains large solvent accessible voids in which residual peaks of diffraction were observed. Complete crystal structure results as CIF files including bond lengths, angles, and atomic coordinates are deposited as Supporting Information. They have been deposited in the Cambridge Structural Database as CCDC1830437 ($\text{Dy}_2\text{H}_2\text{SQ}$) and CCDC1830438 (Dy_2Q).

Magnetic measurements. The dc magnetic susceptibility measurements were performed on solid samples with a Quantum Design MPMS-XL SQUID magnetometer between 2 and 300 K in applied magnetic field of 0.02 T for temperatures of 2-20 K, 0.2 T between 20 and 80 K and 1T for higher temperatures than 80 K. The microcrystallites are immobilized in a pellet made with Teflon tape. The measurements were all corrected for the diamagnetic contribution as calculated with Pascal's constants. The ac magnetic susceptibility measurements were performed on a Quantum Design MPMS-XL SQUID for frequencies between 0.01 and 1000 Hz and a Quantum Design PPMS magnetometers for frequencies between 1000 and 10000 Hz. For the CTM measurements, a single crystal was attached to a square acetate foil with silicon vacuum grease, and its faces were indexed using a SCD Oxford Xcalibur3 X-ray diffractometer. The main part of the instrument consisted of a home-made two-legged CuBe cantilever separated by 0.1 mm from a gold plate. The cantilever was inserted into an Oxford Instruments MAGLAB2000 platform with automated rotation in a vertical magnet. The magnetometer can switch the magnetic field between 0 and 12 T and the temperature between 2 and 300 K. The capacitance was detected with an Andeen-Hagerling 2500A Ultra Precision Capacitance Bridge.

Computational details. Quantum chemical calculations were realized on model complexes of $\text{Dy}_2\text{H}_2\text{SQ}$ and Dy_2Q , namely $[\text{Dy}_1\text{HSQ}]$, $[\text{Dy}_2\text{HSQ}]$ and DyQ respectively (Fig. 7). For both models, the atomic positions were extracted from the X-ray crystal structures and the butyl moieties located on the benzene rings of the TTF have been replaced by hydrogen atoms. The optimization of the hydrogen and fluorine positions, while other atomic positions were kept frozen, have been carried out on the Y^{III} parent molecules by Density Functional Theory (DFT) as implemented in the Gaussian 09 (revision D.01) package⁴¹ using the PBE0 hybrid functional.^{42,43} The « Stuttgart/Dresden » basis sets and effective core potentials were used to describe the yttrium atom⁴⁴ while other atoms were described with the SVP basis sets.⁴⁵ Wavefunction-based calculations were carried out on the optimized molecular structures (replacing one of the Dy^{III}

ions by Y^{III}) by using the SA-CASSCF/RASSI-SO approach, as implemented in the MOLCAS quantum chemistry package (versions 8.0).⁴⁶ In this approach, the relativistic effects are treated in two steps on the basis of the Douglas–Kroll Hamiltonian. First, the scalar terms were included in the basis-set generation and were used to determine the spin-free wavefunctions and energies in the complete active space self-consistent field (CASSCF) method.⁴⁷ Next, spin-orbit coupling was added within the restricted-active-space state-interaction (RASSI-SO) method, which uses the spin-free wavefunctions as basis states.^{48,49} The resulting wavefunctions and energies are used to compute the magnetic properties and g-tensors of the lowest states from the energy spectrum by using the pseudospin $S = 1/2$ formalism in the SINGLE_ANISO routine.^{50,51} The dipolar interactions and J constants are investigated using the POLY_ANISO software, the interaction Hamiltonian is built on the basis of the ground-state doublet of each Dy^{III} center.^{34,52} Cholesky decomposition of the bielectronic integrals was employed to save disk space and speed-up the calculations.⁵³ The active space of the self-consistent field (CASSCF) method consisted of the nine $4f$ electrons of the Dy^{III} ion spanning the seven $4f$ orbitals, i.e. CAS(9,7)SCF. State-averaged CASSCF calculations were performed for all of the sextets (21 roots), all of the quadruplets (224 roots), and 300 out of the 490 doublets (due to software limitations) of the Dy^{III} ion. 21 sextets, 128 quadruplets, and 107 doublets were mixed through spin-orbit coupling in RASSI-SO. All atoms were described by ANO-RCC basis sets.⁵⁴⁻⁵⁶ The following contractions were used: [8s7p4d3f2g1h] for Dy atoms, [7s6p4d2f] for Y atoms, [4s3p2d] for O atoms, [3s2p] for C atoms, [4s3p] for S atoms and [2s] for H atoms.

To give more insights on the orientation of the magnetic axis, the molecular electrostatic potential is calculated from the *ab-initio* LOPROP charge analysis²⁷, using the home-made CAMMEL code (Calculated Molecular Multipolar Electrostatics), following:

$$V(r_i) = \sum_i^N \frac{q_i}{|r_i - r|} + \frac{p_i \cdot r_i}{|r_i - r|^3} + \frac{r_i \cdot (Q_i \times r_i)}{|r_i - r|^5}$$

where q_i , p_i , Q_i and r_i are respectively the charge, dipole and quadrupole moments and displacement vector of the i -th atom. The potential is drawn on a sphere defined by the user around the central lanthanide ion. For a clearer representation of the potential, the intensity can be directly related to both the color (red = high potential and blue = low potential) and the height of the irregularities. Our software enables also to plot the contribution of each component to the total molecular potential. This program has already been used in previous works to give some hints on the orientation of magnetization.^{28,29}

The dipole-dipole interaction⁵⁵ between two magnetic centers 1 and 2, bearing the magnetic moment μ_1 and μ_2 respectively, is described as

$$H_{dip} = -\frac{1}{R_{12}^3} \mu_1 \cdot \mu_2 - 3(\mu_1 \cdot \vec{r}_{12})(\mu_2 \cdot \vec{r}_{12})$$

where R_{12} corresponds to the distance between the magnetic centers and \vec{r}_{12} stands for the unit vector along the 12 direction.

Conflicts of interest

There are no conflicts to declare.

Acknowledgements

This work was supported by the CNRS, Université de Rennes 1, Agence Nationale de la Recherche (N° ANR-13-BS07-0022-01), France-Russia MULTISWITCH PRC Grant (N°227606), the European Commission through the ERC-CoG 725184 MULTIPROSM (project n. 725184) and the Russian Foundation for Basic Research (grant 19-53-15007 NCNI_a). B.L.G. and V.M. thank the French GENCI/IDRIS-CINES centres for high-performance computing resources.

Notes and references

- 1 R. Sessoli, D. Gatteschi, A. Caneschi and M. Novak, Magnetic bistability in a metal-ion cluster, *Nature*, 1993, **365**, 141-143.
- 2 M. Mannini, F. Pineider, P. Saintavit, C. Danieli, E. Otero, C. Sciancalepore, A. M. Talarico, M.-A. Arrio, A. Cornia, D. Gatteschi and S. Sessoli, Magnetic memory of a single-molecule quantum magnet wired to a gold surface, *Nat. Mater.*, 2009, **8**, 194-197.
- 3 S. Thiele, F. Balestro, R. Ballou, S. Klyatskaya, M. Ruben and W. Wernsdorfer, Electrically driven nuclear spin resonance in single-molecule magnets, *Science*, 2014, **344**, 1135-1138.
- 4 K. S. Pedersen, A.-M. Ariciu, S. McAdams, H. Weihe, J. Bendix, F. Tuna and S. Piligkos, Toward Molecular 4f Single-Ion Magnet Qubits, *J. Am. Chem. Soc.*, 2016, **138**, 5801-5804.
- 5 (a) F.-S. Guo, B.-M. Day, Y.-C. Chen, M.-L. Tong, A. Mansikkamäki, and R. A. Layfield, A Dysprosium Metallocene Single-Molecule Magnet Functioning at the Axial Limit, *Angew. Chem., Int. Ed.*, 2017, **56**, 11445-11449; (b) C. A. P. Goodwin, F. Ortu, D. Reta, N. F. Chilton and D. P. Mills, Molecular magnetic hysteresis at 60 kelvin in dysprosocenium, *Nature*, 2017, **548**, 439-442; (c) K. R. McClain, C. A. Gould, K. Chakarawet, S. J. Teat, T. J. Groshens, J. R. Long and B. G. Harvey, High temperature magnetic blocking and magneto-structural correlations in a series of dysprosium(iii) metallocenium single-molecule magnets, *Chem. Sci.*, 2018, **9**, 8492-8503; (d) F.-S. Guo, B.-M. Day, Y.-C. Chen, M.-L. Tong, A. Mansikkamäki and R. A. Layfield, Magnetic hysteresis up to 80 kelvin in a dysprosium metallocene single-molecule magnet, *Science*, 2018, **362**, 1400-1403.
- 6 (a) O. Sato, Dynamic molecular crystals with switchable physical properties, *Nat. Chem.*, 2016, **8**, 644-656; (b) O. Cador, B. Le Guennic and F. Pointillart, Electro-activity and magnetic switching in lanthanide-based single-molecule magnets, *Inorg. Chem. Front.* 2019, **6**, 3398-3417.
- 7 D.-Q. Wu, D. Shao, X.-Q. Wei, F.-X. Shen, L. Shi, D. Kempe, Y.-Z. Zhang, K. R. Dunbar and X.-Y. Wang, Reversible On-Off Switching of a Single-Molecule Magnet via a Crystal-to-Crystal Chemical Transformation, *J. Am. Chem. Soc.*, 2017, **139**, 11714-11717.
- 8 J. Vallejo, E. Pardo, M. Viciano-Chumillas, I. Castro, P. Amoros, M. Déniz, C. Ruiz-Pérez, C. Yuste-Vivas, J. Krzystek, M. Julve, M. Lloret and J.; Cano, Reversible solvatomagnetic switching

- in a single-ion magnet from an entatic state, *Chem. Sci.*, 2017, **8**, 3694-3702.
- 9 D. Pinkowicz, M. Ren, L.-M. Zheng, S. Sato, M. Hasegawa, M. Morimoto, M. Irie, B. K. Breedlove, G. Cosquer, K. Katoh and M. Yamashita, Control of the Single-Molecule Magnet Behavior of Lanthanide-Diarylethene Photochromic Assemblies by Irradiation with Light, *Chem. Eur. J.*, 2014, **20**, 12502-12513.
 - 10 (a) I.-R. Jeon, L. Sun, B. P. Negru, R. Van Duyne, M. Dinca and T. David Harris, Solid-State Redox Switching of Magnetic Exchange and Electronic Conductivity in a Benzoquinoid-Bridged Mn^{II} Chain Compound, *J. Am. Chem. Soc.*, 2016, **138**, 6583-6590; (b) S. Fortier, J. J. Le Roy, C.-H. Chen, V. Vieru, M. Murugesu, L. F. Chibotaru, D. J. Mindiola and K. G. Caulton, A Dinuclear Cobalt Complex Featuring Unprecedented Anodic and Cathodic Redox Switches for Single-Molecule Magnet Activity, *J. Am. Chem. Soc.*, 2013, **135**, 14670-14678; (c) G. N. Newton, S. Yamashita, K. Hasumi, J. Matsuno, N. Yoshida, M. Nihei, T. Shiga, M. Nakano, H. Nojiri, W. Wernsdorfer and H. Oshio, Redox-Controlled Magnetic {Mn₁₃} Keggin Systems, *Angew. Chem. Int. Ed.*, 2011, **50**, 5716-5720; (d) M. Gonidec, E. S. Davies, J. McMaster, D. B. Amabinino and J. Veciana, Probing the Magnetic Properties of Three Interconvertible Redox States of a Single-Molecule Magnet with Magnetic Circular Dichroism Spectroscopy, *J. Am. Chem. Soc.*, 2010, **132**, 1756-1757; (e) L. Norel, M. Feng, K. Bernot, T. Roisnel, T. Guizouarn, K. Costuas and S. Rigaut, Redox Modulation of Magnetic Slow Relaxation in a 4f-Based Single-Molecule Magnet with a 4d Carbon-Rich Ligand, *Inorg. Chem.*, 2014, **53**, 2361-2363; (f) C. M. Dickie, A. L. Laughlin, J. D. Wofford, N. S. Bhuvanesh and M. Nippe, Transition metal redox switches for reversible "on/off" and "slow/fast" single-molecule magnet behaviour in dysprosium and erbium bis-diamidoferrocene complexes, *Chem. Sci.*, 2017, **8**, 8039-8049; (g) B. Lefeuvre, J. Flores Gonzalez, F. Gendron, V. Dorcet, F. Riobé, V. Cherkasov, O. Maury, B. Le Guennic, O. Cador, V. Kuropatov and F. Pointillart, Redox-Modulations of Photophysical and Single-Molecule Magnet Properties in Ytterbium Complexes Involving Extended-TTF Triads, *Molecules*, 2020, **25**, 492506.
 - 11 (a) B. S. Dolinar, S. Gomez-Coca, D. I. Alexandropoulos and K. R. Dunbar, An air stable radical-bridged dysprosium single molecule magnet and its neutral counterpart: redox switching of magnetic relaxation dynamics, *Chem. Commun.*, 2017, **53**, 2283-2286; (b) P. Zhang, M. Perfetti, M. Kern, P. P. Hallmen, L. Ungur, S. Lenz, M. R. Ringenber, W. Frey, H. Stoll, G. Rauhut and J. van Slagaren, Exchange coupling and single molecule magnetism in redox-active tetraxolene-bridged dilanthanide complexes, *J. Chem. Sci.*, 2018, **9**, 1221-1230.
 - 12 (a) T. T. da Cunha, J. Jung, M.-E. Boulon, G. Campo, F. Pointillart, C. L. M. Pereira, B. Le Guennic, O. Cador, K. Bernot, F. Pineider, S. Golhen and L. Ouahab, Magnetic Poles Determinations and Robustness of Memory Effect upon Solubilization in a Dy^{III}-Based Single Ion Magnet, *J. Am. Chem. Soc.*, 2013, **135**, 16332-16335; (b) F. Pointillart, B. Le Guennic, S. Golhen, O. Cador and L. Ouahab, Slow magnetic relaxation in radical cation tetrathiafulvalene-based lanthanide(III) dinuclear complexes, *Chem. Commun.*, 2013, **49**, 11632-11634; (c) F. Pointillart, B. Le Guennic, O. Cador, O. Maury and L. Ouahab, Lanthanide Ion and Tetrathiafulvalene-Based Ligand as a "Magic" Couple toward Luminescence, Single Molecule Magnets, and Magnetostructural Correlations, *Acc. Chem. Res.*, 2015, **48**, 2834-2842.
 - 13 F. Pointillart, S. Klementieva, V. Kuropatov, Y. Le Gal, S. Golhen, O. Cador, V. Cherkasov and L. Ouahab, A single molecule magnet behaviour in a D_{3h} symmetry Dy(III) complex involving a quinone-tetrathiafulvalene-quinone bridge, *Chem. Commun.*, 2012, **48**, 714-716.
 - 14 N. O. Chalkov, V. K. Cherkasov, G. A. Abakumov, G. V. Romanenko, S. Y. Ketkov, I. V. Smolyaninov, A. G. Starikov and V. A. Kuropatov, Compactly Fused *o*-Quinone-Extended Tetrathiafulvalene-*o*-Quinone Triad – a Redox-Amphoteric Ligand, *Eur. J. Org. Chem.*, 2014, 4571-4576.
 - 15 M. Llunell, D. Casanova, J. Cirera, J. M. Bofill, P. Alemany and S. Alvarez, SHAPE (version 2.1), Barcelona, **2013**.
 - 16 A. E. Jones, C. A. Christensen, D. F. Perepichka, A. S. Batsanov, A. Beeby, P. J. Low, M. R. Bryce and A. W. Parker, Photochemistry of the π -Extended 9,10-Bis(1,3-dithiol-2-ylidene)-9,10-dihydroanthracene System: Generation and Characterisation of the Radical Cation, Dication, and Derived Products, *Chem. Eur. J.*, 2001, **7**, 973-978.
 - 17 W. F. Cooper, J. W. Edmonds, F. Wudl and P. Coppens, The 2-2-bi-1,3-dithiole, *Cryst. Struct. Commun.*, 1974, **3**, 23.
 - 18 A. Ellern, J. Bernstein, J. Y. Becker, S. Zamir, L. Shahal and S. Cohen, A New Polymorphic Modification of Tetrathiafulvalene. Crystal Structure, Lattice Energy and Intermolecular Interactions, *Chem. Mater.*, 1994, **6**, 1378-1385.
 - 19 (a) F. Pointillart, Y. Le Gal, S. Golhen, O. Cador and L. Ouahab, Single-Molecule Magnet Behaviour in a Tetrathiafulvalene-Based Electroactive Antiferromagnetically Coupled Dinuclear Dysprosium(III) Complex, *Chem. Eur. J.*, 2011, **17**, 10397-10404; (b) X. Yi, K. Bernot, O. Cador, J. Luzon, G. Calvez, C. Daigebonne and O. Guillou, Influence of ferromagnetic connection of Ising-type Dy^{III}-based single ion magnets on their magnetic slow relaxation, *Dalton Trans.*, 2013, **42**, 6728-6731; (c) F.-S. Guo and R. A. Layfield, Strong direct Exchange coupling and single-molecule magnetism in indigo-bridged lanthanide dimers, *Chem. Commun.*, 2017, **53**, 3130-3133; (d) H. Tian, B.-L. Wang, J. Lu, H.-T. Liu, J. Su, D. Li and J. Dou, Consecutive one-/two-step relaxation transformations of single-molecule magnets via coupling dinuclear dysprosium compounds with chloride bridges, *Chem. Commun.*, 2018, **54**, 12105-12108; (e) L. Zhang, Y.-Q. Zhang, P. Zhang, L. Zhao, M. Guo and J.; Tang, Single-Molecule Magnet Behavior Enhanced by Synergic Effect of Single-Ion Anisotropy and Magnetic Interactions, *Inorg. Chem.*, 2017, **56**, 7882-7889; (f) M. J. Giansiracusa, E. Moreno-Pineda, R. Hussain, R. Marx, M. Martinez Prada, P. Neugebauer, S. Al-Badran, D. Collison, F. Tuna, J. van Slagaren, S. Carretta, T. Guidi, E. J. L. McInnes, R. E. Winpenny and N. F. Chilton, Measurement of Magnetic Exchange in Asymmetric Lanthanide Dimetallics: Toward a Transferable Theoretical Framework, *J. Am. Chem. Soc.*, 2018, **140**, 2504-2513.
 - 20 (a) F. Luis, M. J. Martinez-Pérez, O. Montero, E. Coronado, S. Cardona-Serra, C. Marti-Gastaldo, J.-M. Clemente-Juan, J. Sesé, D. Drung and T. Schurig, Spin-lattice relaxation via quantum tunneling in an Er³⁺-polyoxometalate molecular magnet, *Phys. Rev. B*, 2010, **82**, 060403; (b) F. Pointillart, K. Bernot, S. Golhen, B. Le Guennic, T. Guizouarn, L. Ouahab and O. Cador, Magnetic memory in an isotopically enriched and magnetically isolated mononuclear dysprosium complex, *Angew. Chem. Int. Ed.*, 2015, **54**, 1504-1507; (c) Y. Kishi, F. Pointillart, B. Lefeuvre, F. Riobé, B. Le Guennic, S. Golhen, O. Cador, O. Maury, H. Fujiwara and L. Ouahab, Isotopically enriched polymorphs of dysprosium single molecule magnets, *Chem. Commun.*, 2017, **53**, 3575-3578; (d) E. Moreno-Pineda, M. Damjanovic, O. Fuhr, W. Wernsdorfer and M. Ruben, Nuclear Spin Isomers: Engineering a Et₄N[DyPc₂] Spin Qudit, *Angew. Chem., Int. Ed.*, 2017, **56**, 9915-9919; (e) Y.-C. Chen, J.-L. Liu, W. Wernsdorfer, D. Liu, L. F. Chibotaru, X.-M. Chen and M.-L. Tong, Hyperfine-Interaction-Driven Suppression of Quantum Tunneling at Zero Field in a Holmium(III) Single-Ion Magnet, *Angew. Chem., Int. Ed.*, 2017, **56**, 4996-5000; (f) J. Flores Gonzalez, F. Pointillart and O. Cador, Hyperfine coupling and slow magnetic relaxation in isotopically enriched

- DyIII mononuclear single-molecule magnets, *Inorg. Chem. Front.*, 2019, **6**, 1081-1086.
- 21 X. Zhang, S. Liu, V. Vieru, N. Xu, C. Gao, B. W. Wang, W. Shi, L. F. Chibotaru, S. Gao, P. Cheng and A. K. Powell, Coupling Influences SMM Properties for Pure 4f Systems, *Chem. Eur. J.*, 2018, **24**, 6079-6086.
 - 22 (a) P.-E. Car, M. Perfetti, M. Mannini, A. Favre, A. Caneschi and R. Sessoli, Giant field dependence of the low temperature relaxation of the magnetization in a dysprosium(III)-DOTA complex, *Chem. Commun.*, 2011, **47**, 3751-3753; (b) J.-K. Ou-Yang, N. Saleh, G. Fernandez Garcia, L. Norel, F. Pointillart, T. Guizouarn, O. Cador, F. Totti, L. Ouahab, J. Crassous and B. Le Guennic, Improved slow magnetic relaxation in optically pure helicene-based Dy^{III} single molecule magnets, *Chem. Commun.*, 2016, **52**, 14474-14477.
 - 23 R. Orbach, Spin-lattice relaxation in rare-earth salts, *Proc. R. Soc. Lond. A*, 1961, **264**, 458-484.
 - 24 A. Abragam and B. Bleaney, *B. Electron Paramagnetic Resonance of Transition Ions*, Clarendon Press, Oxford, 1970.
 - 25 A. Singh and K. N. Shrivastava, Optical-acoustic two-phonon relaxation in spin systems, *Phys. Status Solidi B*, 1979, **95**, 273-277; K. N. Shrivastava, Theory of Spin-Lattice Relaxation, *Phys. Status Solidi B*, 1983, **117**, 437-458.
 - 26 J. Tang and P. Zhang, *P. Lanthanide Single Molecule Magnets*; Springer, 2015.
 - 27 L. Gagliardi, R. Lindh and G.; Karlström, Local properties of quantum chemical systems: The LoProp approach, *J. Chem. Phys.*, 2004, **121**, 4494.
 - 28 K. Zhang, V. Montigaud, O. Cador, G.-P. Li, B. Le Guennic, J. Tang, Y. Y. Wang, Tuning the Magnetic Interactions in Dy(III)4 Single-Molecule Magnets, *Inorg. Chem.*, 2018, **57**, 8550-8557.
 - 29 G. Huang, G. Fernandez-Garcia, I. Badiane, M. Camarra, S. Freslon, O. Guillou, C. Daiguebonne, F. Totti, O. Cador, T. Guizouarn, B. Le Guennic and K. Bernot, Magnetic Slow Relaxation in a Metal-Organic Framework Made of Chains of Ferromagnetically Coupled Single-Molecule Magnets, *Chem. Eur. J.*, 2018, **24**, 6983-6991.
 - 30 M. Perfetti, Cantilever torque magnetometry on coordination compounds: from theory to experiments, *Coord. Chem. Rev.*, 2017, **348**, 171-186.
 - 31 I. Mihalcea, M. Perfetti, F. Pineider, L. Tesi, V. Mereacre, F. Wilhelm, A. Rogalev, E. C. Anson, K. A. Powell and R. Sessoli, Spin Helicity in Chain, *Inorg. Chem.*, 2016, **55**, 10068-10074.
 - 32 F. Pointillart, J.-K. Ou-Yang, G. Fernandez Garcia, V. Montigaud, J. Flores Gonzalez, R. Marchal, L. Favereau, F. Totti, J. Crassous, O. Cador, L. Ouahab and B. Le Guennic, Tetrathiafulvalene-Based Helicene Ligand in the Design of a Dysprosium Field-Induced Single-Molecule Magnet, *Inorg. Chem.*, 2019, **58**, 52-56.
 - 33 L. Ungur, M. Thewissen, J.-P. Costes, W. Wernsdorfer and L. F. Chibotaru, Interplay of Strongly Anisotropic Metal Ions in Magnetic Blocking of Complexes, *Inorg. Chem.*, 2013, **52**, 6328-6337.
 - 34 L. F. Chibotaru, L. Ungur, L. The Computer Programs SINGLE_ANISO and POLY_ANISO. 2006, University of Leuven.
 - 35 N. O. Chalkov, V. K. Cherkasov, G. A. Abakumov, G. A. Starikov and A. V. Kuropatov, Protonated paramagnetic redox forms of di-o-quinone bridged with p-phenylene-extended TTF: A EPR spectroscopy study, *Beilstein J. Org. Chem.*, 2016, **12**, 2450-2456.
 - 36 N. O. Chalkov, V. K. Cherkasov, G. A. Abakumov, A. G. Starikov and V. A. Kuropatov, EPR spectroscopy study of di-o-quinone bridged by π -extended TTF: redox behaviour and binding modes as a ligand, *New J. Chem.*, 2016, **40**, 1244-1249.
 - 37 M. F. Richardson, W. F. Wagner and D. E.; Sands. Rare-earth tris(hexafluoroacetyl)acetates and related compounds, *J. Inorg. Nucl. Chem.*, 1968, **30**, 1275-1289.
 - 38 G. L. Sheldrick., SHELXT – Integrated space-group and crystal-structure determination, *Acta Crystallogr. Sect. A Found Adv.*, 2015, **71**, 3-8.
 - 39 G. M. Sheldrick, Crystal structure refinement with SHELXL, *Acta Crystallogr. Sect. C*, 2015, **71**, 3-8.
 - 40 A. L. Spek, Single-crystal structure validation with the program PLATON, *J. Appl. Crystallogr.*, 2003, **36**, 7-13.
 - 41 M. J. Frisch, G. W. Trucks, H. B. Schlegel, G. E. Scuseria, M. A. Robb, J. R. Cheeseman, G. Scalmani, V. Barone, G. A. Petersson, H. Nakatsuji, X. Li, M. Caricato, A. Marenich, J. Bloino, B. G. Janesko, R. Gomperts, B. Mennucci, H. P. Hratchian, J. V. Ortiz, A. F. Izmaylov, J. L. Sonnenberg, D. Williams-Young, F. Ding, F. Lipparini, F. Egidi, J. Goings, B. Peng, A. Petrone, T. Henderson, D. Ranasinghe, V. G. Zakrzewski, J. Gao, N. Rega, G. Zheng, W. Liang, M. Hada, M. Ehara, K. Toyota, R. Fukuda, J. Hasegawa, M. Ishida, T. Nakajima, Y. Honda, O. Kitao, H. Nakai, T. Vreven, K. Throssell, J. A. Montgomery, J. E. Peralta, Jr., F. Ogliaro, M. Bearpark, J. J. Heyd, E. Brothers, K. N. Kudin, V. N. Staroverov, T. Keith, R. Kobayashi, J. Normand, K. Raghavachari, A. Rendell, J. C. Burant, S. S. Iyengar, J. Tomasi, M. Cossi, J. M. Millam, M. Klene, C. Adamo, R. Cammi, J. W. Ochterski, R. L. Martin, K. Morokuma, O. Farkas, J. B. Foresman and D. J. Fox. Gaussian 09. Revision D.01; Gaussian Inc.: Wallingford, CT. 2016.
 - 42 J. P. Perdew, K. Burke and M.; Ernzerhof, Generalized Gradient Approximation, *Phys. Rev. Lett.*, 1996, **77**, 3865.
 - 43 C. Adamo and V. Barone, Toward reliable density functional methods without adjustable parameters: The PBE0 model, *J. Chem. Phys.*, 1999, **110**, 6158.
 - 44 M. Dolg, H. Stoll and H. Preuss, A combination of quasirelativistic pseudopotential and ligand field calculations for lanthanoid compounds, *Theor. Chim. Acta*, 1993, **85**, 441-450.
 - 45 F. Weigend and R. Ahlrichs, Balanced basis sets of split valence, triple zeta valence and quadruple zeta valence quality for H to Rn: Design and assessment of accuracy, *Phys. Chem. Chem. Phys.*, 2005, **7**, 3297-3305.
 - 46 F. Aquilante, J. Autschbach, R. K. Carlson, L. F. Chibotaru, M. G. Delcey, L. De Vico, I. F. Galván, N. Ferré, L. M. Frutos, L. Gagliardi, M. Garavelli, A. Giussani, C. E. Hoyer, G. L. Manni, H. Lischka, D.-X. Ma, P. Malmqvist; T. Müller, A. Nenov, M. Olivucci, T. B. Pedersen, D. L. Peng, F. Plasser, B. Pritchard, M. Reiher, I. Rivalta, I. Schapiro, J. Segarra-Martí, M. Stenrup, D. G. Truhlar, L. Ungur, A. Valentini, S. Vancioillie, V. Veryazov, V. P. Vysotskiy, O. Weingart, F. Zapata and R. Lindh, MOLCAS 8: New capabilities for multiconfigurational quantum chemical calculations across the periodic table, *J. Comput. Chem.*, 2016, **37**, 506-541.
 - 47 B. O. Roos, P. R. Taylor and P. E. M. Siegbahn, A complete active space SCF method (CASSCF) using a density matrix formulated super-CI approach, *Chem. Phys.*, 1980, **48**, 157-173.
 - 48 P. A. Malmqvist, B. O. Roos and B. Schimmelpfennig, The restricted active space (RAS) state interaction with spin-orbit coupling, *Chem. Phys. Lett.*, 2002, **357**, 230-240.
 - 49 P. A. Malmqvist and B. O. Roos, The CASSCF state interaction method, *Chem. Phys. Lett.*, 1989, **155**, 189-194.
 - 50 L. F. Chibotaru and L. Ungur, ab initio calculation of anisotropic magnetic properties of complexes. I. Unique definition of pseudospin Hamiltonians and their derivation, *J. Chem. Phys.*, 2012, **137**, 064112.
 - 51 L. F. Chibotaru, L. Ungur and A. Soncini, The origin of nonmagnetic Kramers doublets in the ground state of dysprosium triangles: evidence for a toroidal magnetic moment, *Angew. Chem. Int. Ed.*, 2008, **47**, 4126-4129.
 - 52 N. Iwahara and L. F. Chibotaru, Exchange interaction between J multiplets, *Phys. Rev. B.*, 2015, **91**, 174438.

- 53 F. Aquilante, P.-A. Malmqvist, T.-B. Pedersen, A. Ghosh. B. O. Roos, Cholesky Decomposition-Based Multiconfiguration Second-Order Perturbation Theory (CD-CASPT2): Application to the Spin-State Energetics of $\text{Co}^{\text{III}}(\text{diiminato})(\text{NPh})$, *J. Chem. Theory Comput.*, 2008, **4**, 694-702.
- 54 B. O. Roos, R. Lindh, P.-A. Malmqvist, V. Veryazov and P.-O. Widmark, Main Group Atoms and Dimers Studied with a New Relativistic ANO Basis Set, *J. Phys. Chem. A*, 2004, **108**, 2851-2858.
- 55 B. O. Roos, R. Lindh, P.-A. Malmqvist, V. Veryazov and P.-O. Widmark, New Relativistic ANO Basis Sets for Transition Metal Atoms, *J. Phys. Chem. A*, 2005, **109**, 6575-6579.
- 56 B. O. Roos, R. Lindh, P.-A. Malmqvist, V. Veryazov, P.-O. Widmark and A.-C. Borin, New Relativistic Atomic Natural Orbital Basis Sets for Lanthanide Atoms with Applications to the Ce Diatom and LuF_3 , *J. Phys. Chem. A*, 2008, **112**, 11431-11435.